Journal of Solid State Chemistry 184 (2011) 1405–1414

Contents lists available at ScienceDirect

Journal of Solid State Chemistry

journal homepage: www.elsevier.com/locate/jssc

Structure and photoluminescence properties of Ce^{3+}-doped novel silicon-oxynitride $Ba_{4-z}M_zSi_8O_{20-3x}N_{2x}$ (M=Mg, Ca, Sr)

Y. Fang [a], Y.Q. Li [a,b,*], R.J. Xie [b], N. Hirosaki [b], T. Takade [b], X.Y. Li [a], T. Qiu [a]

[a] College of Materials Science and Engineering, Nanjing University of Technology, New Model Road 5, Nanjing, Jiangsu 210009, China
[b] Nitride Particle Group, Nano Ceramics Center, National Institute for Materials Science, Namiki 1-1, Tsukuba, Ibaraki 305-0044, Japan

ARTICLE INFO

Article history:
Received 1 January 2011
Received in revised form
21 March 2011
Accepted 26 March 2011
Available online 13 April 2011

Keywords:
Alkaline earth silicon-oxynitride
Cerium
Crystal structure
Luminescence properties
Thermal quenching

ABSTRACT

Structural and photoluminescence properties of undoped and Ce^{3+}-doped novel silicon-oxynitride phosphors of $Ba_{4-z}M_zSi_8O_{20-3x}N_{2x}$ (M=Mg, Sr, Ca) are reported. Single-phase solid solutions of $Ba_{4-z}M_zSi_8O_{20-3x}N_{2x}$ oxynitride were synthesized by partial substitutions of $3O^{2-} \rightarrow 2N^{3-}$ and $Ba \rightarrow M$ (M=Mg, Ca, Sr) in orthorhombic $Ba_2Si_4O_{10}$. The influences of the type of alkaline earth ions of M, the Ce^{3+} concentration on the photoluminescence properties and thermal quenching behaviors of $Ba_3MSi_8O_{20-3x}N_{2x}$ (M=Mg, Ca, Sr, x=0.5) were investigated. Under excitation at about 330 nm, $Ba_3MSi_8O_{20-3x}N_{2x}$:Ce^{3+} (x=0.5) exhibits efficient blue emission centered at 400–450 nm in the range of 350–650 nm owing to the $5d \rightarrow 4f$ transition of Ce^{3+}. The emission band of Ce^{3+} shifts to long wavelength by increasing the ionic size of M due to the modification of the crystal field, as well as the Ce^{3+} concentrations due to the Stokes shift and energy transfer or reabsorption of Ce^{3+} ions. Among the silicon-oxynitride phosphors of $Ba_3MSi_8O_{18.5}N$:Ce^{3+}, $M=Sr_{0.6}Ca_{0.4}$ possesses the best thermal stability probably related to its high onset of the absorption edge of Ce^{3+}.

1. Introduction

Since metal–silicon-oxynitride compounds have been found to be novel hosts of luminescent materials, rare earth activated silicon-oxynitride phosphors have been extensively studied in recent years due to their high potential applications for LED lighting and display [1–4]. In metal silicon-oxynitrides, alkaline earth silicon-oxynitride phosphors have been drawn much more attention because of their high efficiency and high chemical and thermal stability for use as wavelength conversion phosphors for near-UV and blue-LED devices [5–8]. Under UV and blue light excitation, Eu^{2+}-doped alkaline earth silicon-oxynitride materials can emit blue to yellow light, depending on the type of alkaline earth ions and the crystal structure. For example, $MSi_2O_2N_2$:Eu^{2+} emits greenish-yellow light (~560 nm) for M=Ca, green light (~540 nm) for M=Sr, and blue-green light (~500 nm) for M=Ba [6]. As an oxygen-rich oxynitride phosphor, $Ba_3Si_6O_{12}N_2$:Eu^{2+} shows green emission at about 525 nm with a peak width (FWHM) of about 68 nm [9]. Whereas as a nitrogen-rich oxynitride phosphor $BaSi_6N_8O$:Eu^{2+} is a blue-green emitting phosphor with emission peak at about 500 nm [10] due to a different crystal structure. In contrast, Ce^{3+}-doped alkaline earth silicon-oxynitride only shows blue emission and the absorption of Ce^{3+} is normally limited in UV region; for example, under excitation in UV range (300–360 nm), $MSi_2O_2N_2$:Ce^{3+} emits UV-blue and blue light with a broad emission band peaking at about 392, 396, and 473 nm for M=Ca, Ba, and Sr, respectively [11]. Similar to oxide based phosphors, in comparison with Eu^{2+} the $5d \leftrightarrow 4f$ transition of Ce^{3+} is always located at higher energy in alkaline earth silicon oxynitride phosphors in the same hosts.

Recently, a few investigations have been reported about the preparation of oxynitride phosphors through the approaches of the cross-substitution of $(AlO)^+ \rightarrow (SiN)^+$, as well as the unequivalent substitution of $3O^{2-} \rightarrow 2N^{3-}$, starting from the oxide based hosts, such as alkaline earth aluminosilicate and alkaline earth silicate compounds [12–15]. From a structural viewpoint, a large number of alkaline earth silicates are highly promising to be incorporated by nitrogen into the silicate host lattices to form new silicon-oxynitride materials, which enables us to use them as novel hosts of luminescent materials.

In the present work, we selected an oxide-based orthorhombic $Ba_2Si_4O_{10}$ [16] or $BaSi_2O_5$ [17] as a mother compound and then partially replaced oxygen by nitrogen using Si_3N_4 as nitrogen source. To our best knowledge, apart from several studies on the luminescence properties of $BaSi_2O_5$:Eu^{2+} [18] (with similar crystal structure of $Ba_2Si_4O_{10}$ [16,17]), the

---

* Corresponding author at: College of Materials Science and Engineering, Nanjing University of Technology, New Model Road 5, Nanjing, Jiangsu 210009, China

E-mail address: y.q.li@njut.edu.cn (Y.Q. Li).

0022-4596/$ - see front matter © 2011 Elsevier Inc. All rights reserved.
doi:10.1016/j.jssc.2011.03.048

photoluminescence properties of Ce^{3+}-doped silicon-oxynitride based on the orthorhombic structure of $Ba_2Si_4O_{10}$ by partial replacement of O with N have not yet been reported so far. Therefore, in this work we investigate on the synthesis of Ce^{3+}-doped $Ba_{4-z}M_zSi_8O_{20-3x}N_{2x}$ $(0 \le x \le 1)$ (M=Mg, Ca, Sr) by a solid state reaction at high temperature using alkaline earth carbonates, silicon nitride, silicon oxide and cerium oxide as raw materials. The phase formation and the crystal structure were analyzed by X-ray powder diffraction. The microstructure of the phosphors was observed by scanning electron microscopy. Subsequently, the photoluminescence properties and the thermal stability of Ce^{3+}-doped oxynitride phosphors have been discussed in detail.

2. Experimental procedures

2.1. Synthesis

Undoped and Ce^{3+}-doped alkaline earth silicon-oxynitride phosphors of $Ba_{4-z}M_zSi_8O_{20-3x}N_{2x}$ were prepared by a solid state reaction with the starting material of Si_3N_4 (SN-E10, Ube Industries, Ltd., Tokyo, Japan), SiO_2 (Kojundo, Chemical Laboratory Co. Ltd., Japan), $BaCO_3$ (Sigma-Aldrich, 99.5%), MgO (Konoshima Chemical Co. Ltd., Osaka, Japan), $CaCO_3$ (Kojundo, Chemical Laboratory Co. Ltd., Japan), $SrCO_3$ (Sigma-Aldrich, 99.95%), and CeO_2 (Shin-Etsu Chemical Co. Ltd., Japan, purity $>99.99\%$). The concentration of the activator ion of Ce^{3+} in $Ba_{4-z}M_zSi_8O_{20-3x}N_{2x}$ is set as related to the total molar amounts of Ba and M. The appropriate amounts of raw materials were weighed out according to the stoichiometric formulations and then homogeneously mixed in a silicon-nitride mortar and pestle. The powder mixtures were pressed into a pellet and fired in a BN boat at 1050–1300 °C in a horizontal tube furnace under a firing atmosphere of N_2–H_2 (5%). The firing temperature depends on the composition and the activator concentration of Ce^{3+}. After firing, the samples were cold down to room temperature in the furnace and then ground into powder for the subsequent characterizations.

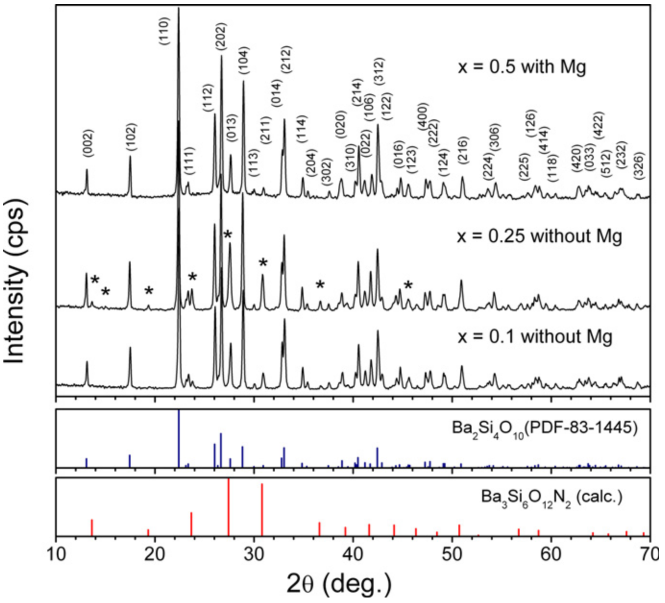

Fig. 1. X-ray powder diffraction patterns of $Ba_{4-z}Mg_zSi_8O_{20-3x}N_{2x}$ (from bottom to top z=0, 0, and 1). The asterisks indicate the impurity phase of $Ba_3Si_6O_{12}N_2$.

2.2. Characterizations

The phase formation of the synthesized materials was analyzed by X-ray powder diffraction (XRD) carried out at the condition of 40 kV and 40 mA with Cu$K\alpha$ radiation (RINT 2000, Ultima III, Rigaku, Japan) in the 2θ range of 10–70° by normal scanning with the speed of 2°/min. As regard to the Rietveld refinements, the data were collected by a step scanning mode with a step size of 0.02° and a count time of 6 s per step in the range of 10–100°. The Rietveld refinements were carried out by the GSAS package [19,20]. The structural parameters of a single crystal $Ba_2Si_4O_{10}$ [16] were adopted as an initial model for the refinement of the crystal structure of $Ba_{4-z}M_zSi_8O_{20-3x}N_{2x}$ (x=0.5, z=1). The Ce and N ions are supposed to be randomly occupied on Ba and O sites in $Ba_2Si_4O_{10}$, respectively, in the course of the Rietveld refinements.

The morphology and particle size of the silicon-oxynitride phosphor were observed by scanning electron microscopy (JEOL, JSM-5900, Japan).

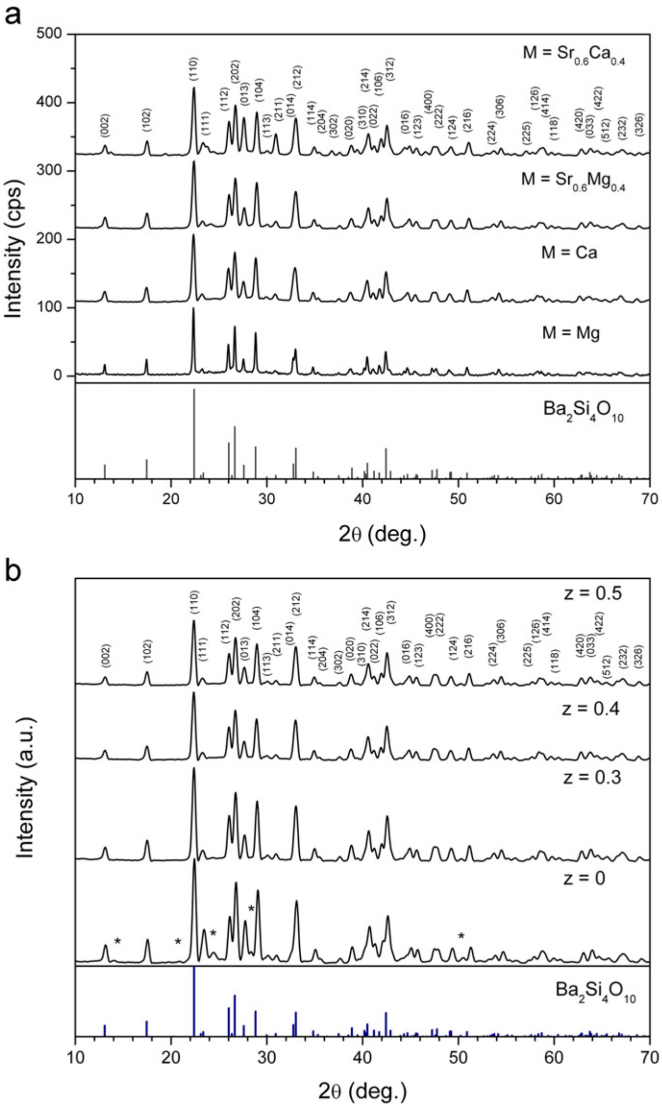

Fig. 2. (a) X-ray powder diffraction patterns of $Ba_{2.94}MCe_{0.04}Si_8O_{18.5}N$ (Ce=1 mol%, M=Mg, Ca, $Sr_{0.6}Mg_{0.4}$, $Sr_{0.6}Ca_{0.4}$). (b) X-ray powder diffractions of $Ba_{2.94}Sr_{1-z}Mg_zCe_{0.04}Si_8O_{18.5}N$ at different z (the asterisks are the impurity phase of $Ba_3Si_6O_{12}N_2$).

The photoluminescence spectra of the samples were measured by a fluorescent spectrophotometer (Model F-4500, Hitachi Ltd., Japan) with a 150 W Ushio xenon short arc lamp at room temperature. The emission spectrum was corrected for the spectral response of a monochromator and Hamamatsu R928P photomultiplier tube by a light diffuser and tungsten lamp. The excitation spectrum was corrected for the spectral distribution of xenon lamp intensity by measuring rhodamine-B as a reference. The diffuse reflection spectrum was measured by a UV–vis spectrophotometer (JASCO, V-560, Japan) using $BaSO_4$ white plate as a standard reference.

The temperature-dependent luminescence properties and quantum efficiency were recorded on an intensified Multichannel Spectrophotometer (Otsuka Electrics MCPD-7000, Japan) with a 200 W Xe-lamp as an excitation source. The temperature-dependent luminescence of the samples was measured from the room temperature to 250 °C with a heating rate of 100 °C/min, and the dwell time of 5 min at each preset temperature.

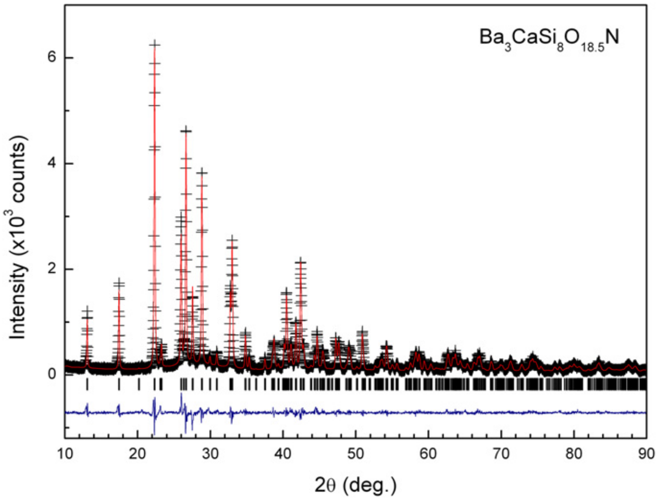

Fig. 3. Rietveld refinement X-ray powder diffraction patterns of undoped $Ba_3CaSi_8O_{18.5}N$. Cross is the observed pattern; solid line is the calculated pattern; the curve at the bottom is the difference between the observed and the calculated patterns. The vertical bars are the Bragg diffraction lines of orthorhombic $Ba_2Si_4O_{10}$.

Table 1
Crystal structure data for $Ba_3CaSi_8O_{18.5}N$ (standard deviations in parentheses).

Formula		$Ba_3CaSi_8O_{18.5}N$				
Formula weight		986.74				
Crystal system		Orthorhombic				
Space group		*Pmcn* (No. 62)				
Lattice parameters		a=7.6843(1) Å				
		b=4.6417(1) Å				
		c=13.5080(4) Å				
		V=481.81(1) Å^3				
Z		2				
Density (calc.)		3.401 g/cm^3				
R_{wp}		9.6%				
R_p		7.4%				
$\chi 2$		1.5				
Atom	wyck.	x/a	y/b	z/c	S.O.F.	U (100 × Å^2)
Ba/Ca	4*c*	0.2500	0.7820(4)	0.5441(1)	0.75/0.25	1.61
Si1	8*d*	0.4550(5)	0.8587(9)	0.8183(3)	1.00	2.44
O/N1	4*c*	0.2500	0.9532(22)	0.8401(7)	0.925/0.05	1.59
O/N2	8*d*	0.5381(9)	0.7409(21)	0.9160(4)	0.925/0.05	1.93
O/N3	8*d*	0.4475(9)	0.6563(17)	0.7149(6)	0.925/0.05	1.92

S.O.F.=site occupancy fraction.

3. Results and discussion

3.1. Phase formation and structural characterization

According to the designed formulation of blank $Ba_4Si_8O_{20-3x}N_{2x}$, it was found that the solid solubility of nitrogen was significantly low for forming a single phase solid solution. The maximum x value was only about 0.05 for $Ba_4Si_8O_{20-3x}N_{2x}$ with sole alkaline earth ion of Ba in the host. Incorporating more nitrogen in $Ba_2Si_4O_{10}$ resulted in forming another impurity $Ba_3Si_6O_{12}N_2$-like phase [9] instead of forming a solid solution (see the marked asterisks in Fig. 1). Therefore, without the substitution of other alkaline earth ions, viz. Mg, Ca, and Sr, only substitution of O with N was found very difficult to be incorporated into pure $Ba_2Si_4O_{10}$ host lattice, as shown in Fig. 1. While partial substitution of Ba for Mg, Ca, and/or the combination of Sr with Mg or Ca can significantly improve the solid solubility of nitrogen up to x=0.5 in the $Ba_2Si_4O_{10}$ lattice. In this way, the solid solutions with relatively high nitrogen content were readily

Table 2
Selected bond length (in Å) and bond angles (°) of $Ba_3CaSi_8O_{18.5}N$ (standard deviations in parentheses).

[(Ba/Ca)(O/N)$_7$] polyhedra	
Ba/Ca1–O/N1	2.964(9)
Ba/Ca1–O/N2	2.812(6) × 2
Ba/Ca1–O/N2	2.735(9) × 2
Ba/Ca1–O/N3	2.823(6) × 2
Mean	2.815
[Si(O/N)$_4$] tetrahedra	
Si1–O/N1	1.661(4)
Si1–O/N2	1.564(7)
Si1–O/N3	1.684(8)
Si1–O/N3	1.635(7)
Mean	1.636
O/N–Si–O/N angles	
O/N1–Si1–O/N2	109.3(5)
O/N1–Si1–O/N3	105.1(5)
O/N2–Si1–O/N3	121.2(5)
O/N2–Si1–O/N3	109.9(5)
O/N3–Si1–O/N3	105.01(27)

obtained, particularly for the smaller ions of Mg^{2+} and Ca^{2+}. Fig. 2(a) shows the observed X-ray powder diffraction patterns of $Ba_{2.94}MCe_{0.04}Si_8O_{18.5}N$ (M=Mg, Ca, $Sr_{0.6}Mg_{0.4}$, $Sr_{0.6}Ca_{0.4}$). It is clear that the observed XRD patterns perfectly match with the host lattice of $Ba_2Si_4O_{10}$, which means the N^{3-} and Ce^{3+} ions can be incorporated into the host lattice of $Ba_2Si_4O_{10}$ substituted for O^{2-} and Ba^{2+}, respectively. With an increase of the ionic radius of the M ions going from Mg via Ca to Sr, the solid solubility of N in $Ba_2Si_4O_{10}$ slightly decreases for a large Sr atom (for example at x=0.5). As a result, a small amount of Mg or Ca have to be co-substituted with Sr (e.g., M=$Sr_{0.6}Mg_{0.4}$ and M=$Sr_{0.6}Ca_{0.4}$) in order to maintain the stability of the orthorhombic structure with high amounts of N in the host. This effect can be seen clearly from the X-ray powder diffraction patterns of Fig. 2(b), in which only when $z \geq 0.3$ in $Ba_{2.94}Sr_{1-z}Mg_zCe_{0.04}Si_8O_{18.5}N$, a nearly single-phase solid solution can be obtained. This synthetic approach of co-substitution was also applied to $Ba_3MSi_8O_{18.5}N{:}Ce^{3+}$ (M=$Sr_{0.6}Ca_{0.4}$) as shown in Fig. 2(a). While further incorporation of more nitrogen was found to be presented in more $Ba_3Si_6O_{12}N_2$-like phases (not shown in the XRD patterns).

As typical examples, the crystal structures of $Ba_{4-z}M_zSi_8O_{20-3x}N_{2x}$ (x=0.5, z=1, and M=Ca, $Sr_{0.6}Ca_{0.4}$) were studied in detail for insightfully understanding the silicon-oxynitride solid solutions. Fig. 3 shows the Rietveld refinement X-ray powder diffraction pattern of the host of $Ba_3CaSi_8O_{18.5}N$. The refinement parameters, crystallographic data, and selected interatomic distances and bond angles are summarized in Tables 1 and 2 for $Ba_3CaSi_8O_{18.5}N$ and Tables 3 and 4 for $Ba_3Sr_{0.6}Ca_{0.4}Si_8O_{18.5}N$. In agreement with the refined composition, the oxygen content is about 31.6 wt% and the nitrogen content is about 1.37 wt% determined by chemical analysis, which are close to the theoretical values of 29.99 and 1.42 wt% of $Ba_3CaSi_8O_{18.5}N$.

As a solid solution of a low temperature modification of $Ba_2Si_4O_{10}$ or $BaSi_2O_5$ [16,17], $Ba_3MSi_8O_{18.5}N$ (M=Mg, Ca, $Sr_{0.6}Mg_{0.4}$, $Sr_{0.6}Ca_{0.4}$) is crystallized in an orthorhombic crystal system with the space group *Pmcn* (No. 62). The nitrogen atoms were assumed to be randomly distributed on the crystallographic sites of the oxygen atoms. The hybridized tetrahedra of $[Si(O,N)_4]$ are connected by sharing corners of O/N atoms every two tetrahedra in the unit cell of the chains along (010) to form two single chains, and those chains construct the tetrahedral layers along (001). Fig. 4 shows the typical crystal structure of silicon-oxynitride hosts of $Ba_3MSi_8O_{18.5}N$ (M=Mg, Ca, $Sr_{0.6}Mg_{0.4}$, $Sr_{0.6}Ca_{0.4}$). In between the tetrahedral layers of $[Si(O,N)_4]$, the M (M=Mg, Ca, $Sr_{0.6}Mg_{0.4}$, $Sr_{0.6}Ca_{0.4}$) atoms are occupied on the Ba sites, sharing the Wyckoff position of the 4*c* sites in an orthorhombic lattice. In $Ba_3MSi_8O_{18.5}N$, within the first nearest coordination atoms of O/N, the Ba atom along with M atom is coordinated with seven and nine O/N atoms for M=Ca and M=$Sr_{0.6}Ca_{0.4}$, respectively. The average bond length of Ba/M–O/N is about 2.815 and 2.869 Å for M=Ca and M=$Sr_{0.6}Ca_{0.4}$, respectively (see Tables 2 and 4). Due to the size effect, the average bond length is expectedly shortened by partial replacement of Ba with the small ionic size of M, e.g., Ca and $Sr_{0.6}Ca_{0.4}$, as compared to $Ba_2Si_4O_{10}$ (the average bond length of Ba–O is about 2.8399 Å [16]). The overall lattice does not show marked shrinkage (~0.9%) by the partial replacement of Ba by M, e.g., Ca and $Sr_{0.6}Ca_{0.4}$, probably owing to its $[Si(O,N)_4]$ layered structural character. However, the substitution of Ba for M can obviously change the interatomic distances for Ba/M–O/N and Si–O/N as listed in Tables 2 and 4.

Fig. 5 presents the scanning electron microscopy images of $Ba_3MSi_8O_{20-3x}N_{2x}{:}Ce^{3+}$ (Ce=1 mol%, M=Mg, Ca, $Sr_{0.6}Mg_{0.4}$,

Table 4
Selected bond length (in Å) and bond angles (in °) of $Ba_3Sr_{0.6}Ca_{0.4}Si_8O_{18.5}N$ (Standard deviations in parentheses).

[(Ba/Sr/Ca)(O/N)$_9$] polyhedra	
Ba/Sr/Ca1–O/N1	3.036(12)
Ba/Sr/Ca1–O/N2	3.036(12) × 2
Ba/Sr/Ca1–O/N2	2.806(9) × 2
Ba/Sr/Ca1–O/N2	2.744(11) × 2
Ba/Sr/Ca1–O/N3	2.808(9) × 2
Mean	2.869
[Si(O/N)$_4$] tetrahedra	
Si1–O/N1	1.612(6)
Si1–O/N2	1.582(9)
Si1–O/N3	1.674(11)
Si1–O/N3	1.613(11)
Mean	1.620
O/N–Si–O/N angles	
O/N1–Si1–O/N2	110.5(6)
O/N1–Si1–O/N3	104.1(6)
O/N1–Si1–O/N3	107.6(7)
O/N2–Si1–O/N3	119.4(6)
O/N2–Si1–O/N3	108.3(7)
O/N3–Si1–O/N3	106.3(4)

Table 3
Crystal structure data for $Ba_3Sr_{0.6}Ca_{0.4}Si_8O_{18.5}N$ (standard deviations in parentheses).

Formula	$Ba_3Sr_{0.6}Ca_{0.4}Si_8O_{18.5}N$
Formula weight	1015.27
Crystal system	Orthorhombic
Space group	*Pmcn* (No. 62)
Lattice parameters	a=7.6687(1) Å b=4.6282(1) Å c=13.4485(5) Å V=477.32(1) Å^3
Z	2
Density (calc.)	3.532 g/cm^3
R_{wp}	12.6%
R_p	9.1%
χ^2	4.4

Atom	*wyck.*	*x/a*	*y/b*	*z/c*	S.O.F.	U (100* × Å^2)
Ba/Sr/Ca	4*c*	0.2500	0.7958(5)	0.5446(1)	0.75/0.15/0.1	1.88
Si1	8*d*	0.4512(6)	0.8763(14)	0.8165(4)	1.00	2.16
O/N1	4*c*	0.2500	0.9617(30)	0.8347(9)	0.925/0.05	1.28
O/N2	8*d*	0.5359(12)	0.7563(27)	0.9155(6)	0.925/0.05	1.33
O/N3	8*d*	0.4462(11)	0.6663(25)	0.7151(8)	0.925/0.05	1.05

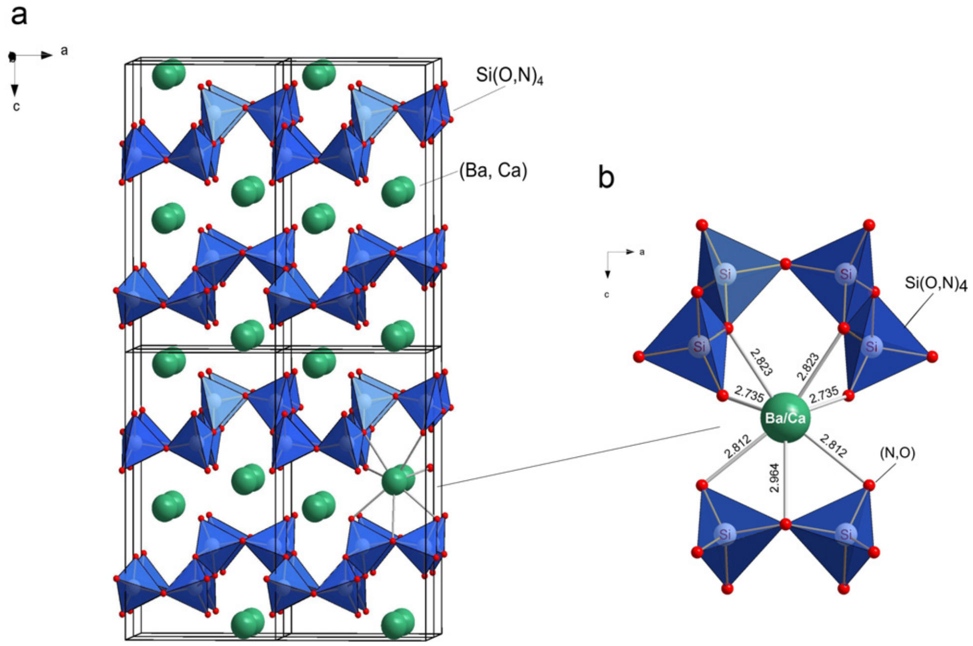

Fig. 4. (a) Perspective crystal structure of oxynitride host of $Ba_3MSi_8O_{18.5}N$ (M=Mg, Ca, Sr) and (b) local coordination of Ba with O/N for $Ba_3CaSi_8O_{18.5}N$ (bond length in Å).

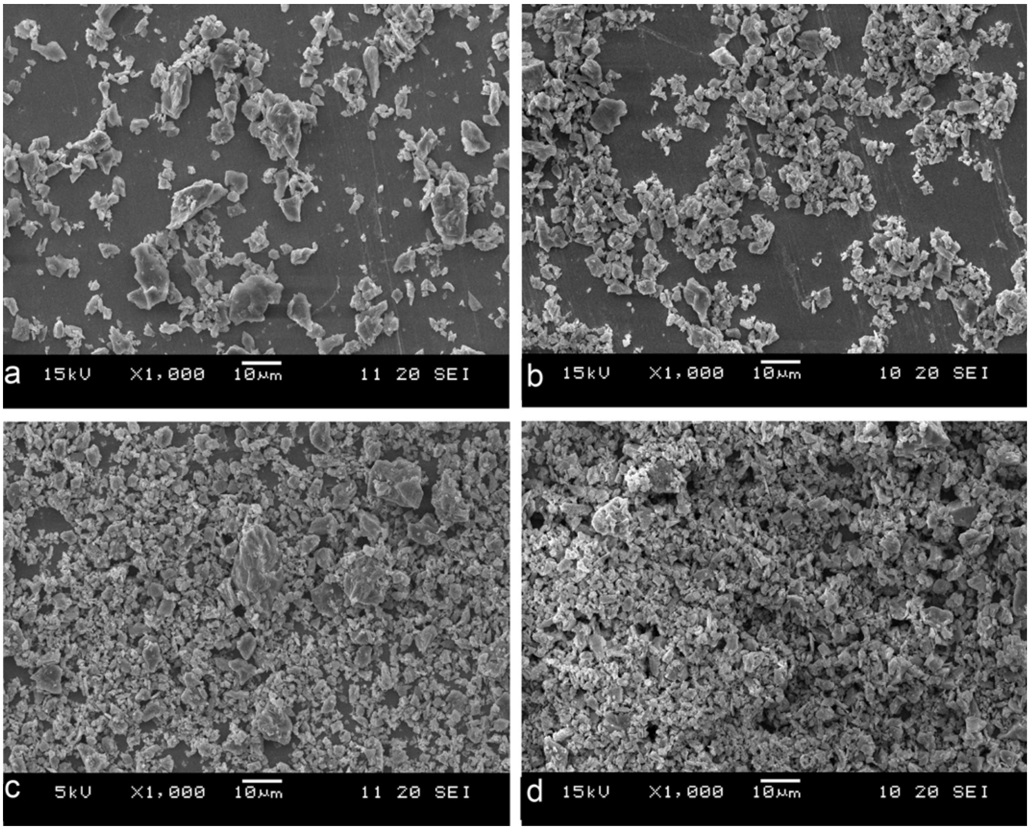

Fig. 5. Scanning electron microscopy images of $Ba_3MSi_8O_{18.5}N{:}Ce^{3+}$ (1 mol%): (a) M=Mg, (b) M=Ca, (c) M=$Sr_{0.6}Mg_{0.4}$, and (d) M=$Sr_{0.6}Ca_{0.4}$.

$Sr_{0.6}Ca_{0.4}$) phosphors. The synthesized silicon-oxynitride phosphor powders are generally consisted of spheroidal particles with a mean diameter approximately to be 2–5 μm. Obviously, some irregular-shaped particles with large particle size above 10 μm can also be observed in Mg-containing oxynitride phosphors. Relatively, the particle size is more homogenous just with a small amount of large particles/agglomerations for M=Ca and $Sr_{0.6}Ca_{0.4}$. A sample of M=Mg has the largest particle size ranging from 2 to

10 μm with some rod-like particles, which could be related to its lower glass-forming temperature that results in abnormal grain growth. With partial replacement of Mg by Sr (as shown Fig. 5c), the particle size becomes small and the distribution becomes narrow as compared to M=Mg. The average particle size is about 5 μm and some large particles still exist. The particle size of M=Ca sample is relatively smaller (~3.8 μm) and more homogeneous. The morphology of the particle is equiaxed-grain (Fig. 5b). Similar to M=Ca, the particle size of $M=Sr_{0.6}Ca_{0.4}$ sample is about 4–5 μm with small amounts of rod-like particles (Fig. 5d).

3.2. Luminescence properties of $Ba_3MSi_8O_{20-3x}N_{2x}:Ce^{3+}$ (M=Mg, Ca, $Sr_{0.6}Mg_{0.4}$, $Sr_{0.6}Ca_{0.4}$)

Fig. 6 shows the diffuse reflection spectra of undoped and Ce^{3+}-doped $Ba_3MSi_8O_{18.5}N$. The undoped $Ba_2Si_4O_{10}$ shows high reflection (>85%) superimposed on the reflection spectra in the spectral range of 500–800 nm and gradually decreases from 500 to 300 nm. In the UV range below 300 nm, a sharp drop in the reflection spectrum can be observed, which corresponds to the valence-to-conduction band transition of the $Ba_2Si_4O_{10}$ host. From the reflection spectrum, a roughly estimated optical bandgap is about 4.6 eV for orthorhombic $Ba_2Si_4O_{10}$. The reflection spectra of Ce^{3+}-doped $Ba_3MCaSi_8O_{18.5}N$ have two broad absorption bands at about 240 and 322 nm. The absorption band at 240 nm is readily assigned to the host lattice excitation due to the valence to conduction band transition that is similar to the host. The absorption band centered at about 322 nm is ascribed to the absorption of the Ce^{3+} ions because of a lack of this band in the reflection spectrum of the host of $Ba_2Si_4O_{10}$. Accordingly, only one broad absorption band of Ce^{3+} exists in $Ba_3MCaSi_8O_{18.5}N:Ce^{3+}$ phosphors originated from the 4f–5d transition of Ce^{3+}. Furthermore, according to the reflection spectra the estimated onset of the absorption edge of Ce^{3+} slightly decreases in a rough sequence of $Sr_{0.6}Ca_{0.4}$–Mg–Ca–$Sr_{0.6}Mg_{0.4}$. Relatively speaking, the absorption edge of $M=Sr_{0.6}Ca_{0.4}$ is located at high energy as shown in Table 5.

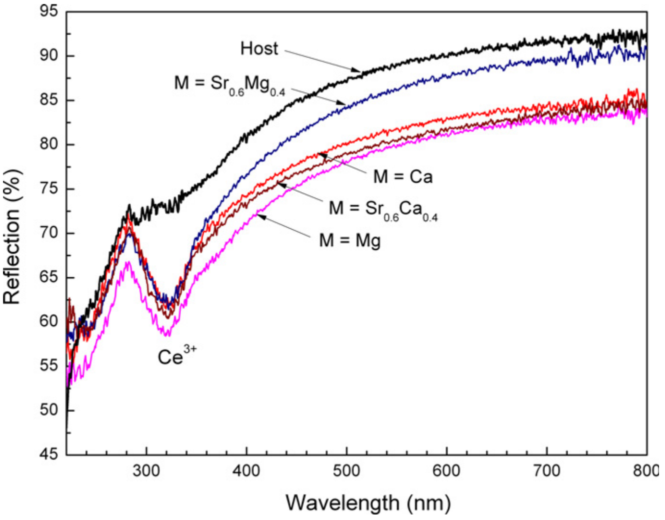

Fig. 6. Diffuse reflection spectra of undoped- and Ce^{3+}-doped $Ba_3MSi_8O_{18.5}N$ (Ce^{3+}=1 mol%, M=Mg, Ca, $Sr_{0.6}Mg_{0.4}$, $Sr_{0.6}Ca_{0.4}$).

Table 5
Luminescence data for $Ba_3MSi_8O_{18.5}N:Ce^{3+}$ (Ce^{3+}=1 mol%, M=Ca, Mg, $Sr_{0.6}Mg_{0.4}$, $Sr0_{.6}Ca_{0.4}$).

	M=Mg	M=Ca	$M=Sr_{0.6}Mg_{0.4}$	$M=Sr_{0.6}Ca_{0.4}$
Excitation max. (nm)	325	334	335	338
Emission max. (nm)	410	413	414	415
Absorption edge (eV)	3.13	3.05	3.08	3.24
Stokes shift (cm^{-1})	6379	5727	5696	5489
Quantum efficiency (%)	38	44	39	38
Thermal quenching $T_{1/2}$ (°C)	144	133	135	171

Fig. 7 illustrates the influence of the Ce^{3+} concentration on the diffuse reflectance spectra of $Ba_3MCaSi_8O_{18.5}N:Ce^{3+}$ with single- and dual-substitution of M (Mg, Ca, $Sr_{0.6}Mg_{0.4}$, and $Sr_{0.6}Ca_{0.4}$) for Ba. As seen from the reflection spectra, the intensity of the absorption band of Ce^{3+} at about 322 nm is gradually enhanced with increasing the Ce^{3+} concentration in all cases. In the meantime, the absorption edge of Ce^{3+} shifts to longer wavelength, i.e., low energy, varying from y=0.04 to 0.16 (i.e., 1–4 mol% Ce^{3+}) as expected. However, the change of the type of M from Mg, Ca, $Sr_{0.6}Mg_{0.4}$ to $Sr_{0.6}Ca_{0.4}$ gives very similar absorption characters of Ce^{3+} without resulting in significant changes, as shown in Figs. 7(a)–(d).

Fig. 8 shows the excitation and emission spectra of $Ba_{2.94}M$-$Ce_{0.04}Si_8O_{18.5}N$ (M=Mg, Ca, $Sr_{0.6}Mg_{0.4}$,$Sr_{0.6}Ca_{0.4}$). In agreement with the reflection spectra, a weak excitation band at short wavelength below 260 nm corresponds to the valence to conduction band transition of the host. A strong broad excitation band centered at about 320–340 nm can be observed in the excitation spectra, which corresponds to the absorption band at about 322 nm of the reflection spectra. This broad excitation band actually is composed of several Gaussian sub-bands of Ce^{3+} (see Fig. 8b), which is attributed to the transition of $4f^15d^0 \rightarrow 5d^1$ of Ce^{3+}. As an example for $Ba_{2.94}CaCe_{0.04}Si_8O_{18.5}N$ phosphor, the deconvolved Gaussians of Ce^{3+} are located at about 264, 303, and 340 nm in the excitation spectrum. The shortest excitation band (in wavelength) centered at 203 nm belongs to the host lattice excitation as mentioned above. Moreover, the excitation maxima show a slight red-shift with the ionic radius of M becoming large in the order of Mg (0.72 Å) < Ca (1.06 Å) ≈ $Sr_{0.6}Mg_{0.4}$ (ca. 1.05 Å) < $Sr_{0.6}Ca_{0.4}$ (ca. 1.15 Å), namely the excitation peak is at about 325 nm for M=Mg, 334 nm for M=Ca, 335 nm for $M=Sr_{0.6}Mg_{0.4}$, and 338 nm for $M=Sr_{0.6}Ca_{0.4}$. When excited under UV to 330 nm, $Ba_{2.94}Ce_{0.04}MSi_8O_{18.5}N$ emits blue light with a broad band peaking at about 410–420 nm varying with the type of M (Table 5). As usual, the asymmetric emission band can be decomposed into the characteristics of double-band emission of Ce^{3+} (i.e., 408 and 458 nm) roughly associated with two ground states of Ce^{3+}, i.e., $^2F_{5/2}$ and $^2F_{7/2}$, having energy difference of about 2600 cm^{-1} in the case of $Ba_{2.94}Ce_{0.04}MSi_8O_{18.5}N$ (Fig. 8b) due to spin–orbit coupling [21]. In relation to the excitation spectra, the M ions have a slight influence on the position of the emission bands, and the emission band of Ce^{3+} also shows small red-shift as the ionic radius of M increases, as given in Table 5. Since the estimated Stokes shift slightly decreases with increase in the ionic size of M (Table 5), the red-shift may be mainly related to the crystal field effects upon the 5d levels of the Ce^{3+} ions due to the modification of the crystal field by the M ions [21,22], as well as the structural relaxation.

Fig. 8c shows the effect of M substitution on the emission intensity of $Ba_{2.94}Ce_{0.04}MSi_8O_{18.5}N$. It is found that Ca containing phosphors have higher emission intensity, which could be related to the size effect due to very similar ionic size between Ce^{3+} (1.07 Å for C.N.=7) and Ca^{2+} (1.06 Å for C.N.=7) [23].

Fig. 9 depicts the photoluminescence properties as a function of the Ce^{3+} concentration. With increase in Ce^{3+} concentration

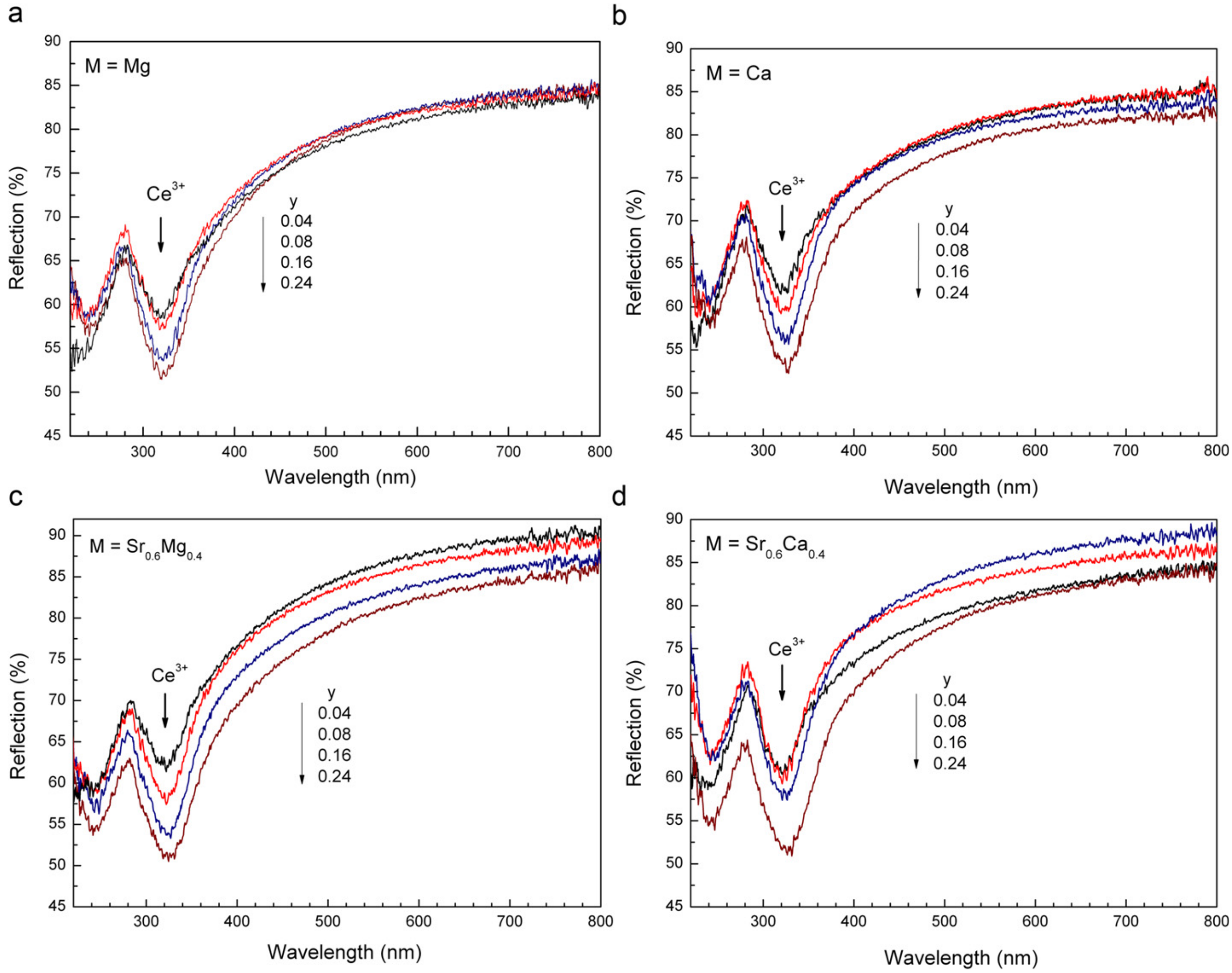

Fig. 7. Diffuse reflection spectra of $Ba_{3-1.5y}MCe_ySi_8O_{18.5}N$ (M=Mg, Ca, $Sr_{0.6}Mg_{0.4}$, $Sr_{0.6}Ca_{0.4}$; y=0.04, 0.08, 0.16, and 0.24).

from 0.5 to 6 mol% (y=0.02–0.24), both the excitation and emission bands of Ce^{3+} shift to long wavelengths. For single-substitution of Ba with Mg (322–339 nm) and Ca (328–345 nm), the red-shift is about 17 nm; for dual-substitution of Ba with $Sr_{0.6}Mg_{0.4}$ (329–339 nm) and $Sr_{0.6}Ca_{0.4}$ (332–342 nm), the red shift is about 10 nm for the excitation bands. Correspondingly, the position of the emission bands also significantly shifts to long wavelengths of about 31–34 nm depending on M, viz., shifting from 404 to 438 nm for M=Mg, 408–439 nm for M=Ca, and 411–444 nm for M=$Sr_{0.6}Mg_{0.4}$ and M=$Sr_{0.6}Ca_{0.4}$ in the blue spectral range of 400–450 nm. Those data are also in agreement with the observed results in Fig. 8 for different Ce^{3+} concentration along with different M ions. With the variation of the Ce^{3+} concentration from 0.5 to 6 mol% (y=0.02–0.24), the Stokes shift indeed shows a slight increase ($<1000\ cm^{-1}$). Therefore, apart from the effect of Stokes shift, the red-shift of the excitation and emission bands can also be attributed to energy transfer and reabsorption between Ce^{3+} and Ce^{3+} ions because the nearest distance between Ce^{3+} and Ce^{3+} becomes short at higher Ce^{3+} concentration, which provides more opportunities for energy transfer [21,22]. In all systems, the luminescent intensity of Ce^{3+} is gradually increased with increasing the Ce^{3+} concentration in the studied composition range and the concentration quenching of Ce^{3+} could not be observed even to form glass products at high Ce^{3+} content. The quantum efficiency of $Ba_3MSi_8O_{18.5}N:Ce^{3+}$ ranges from 34% to 50%, depending on the type of M and Ce concentrations. In good agreement with the emission intensity (Fig. 8c), when the Ce^{3+} concentration is 1 mol%, the quantum efficiency of $Ba_3MSi_8O_{18.5}N:Ce^{3+}$ is about 38%, 44%, 39%, and 38% for Mg, Ca, $Sr_{0.6}Mg_{0.4}$, and $Sr_{0.6}Ca_{0.4}$, respectively (Table 5). It is worth noting that although nitrogen can be incorporated into the oxide lattice of $Ba_2Si_4O_{10}$ to form silicon-oxynitride, the relative ratio of N/O is still low, which implies the crystal field is dominated by oxygen and not nitrogen as in the present silicon-oxynitride phosphors. Therefore, as compared with $Ba_2Si_4O_{10}:Ce^{3+}$ the excitation and emission spectra have no significant change with an increase of N in the lattice.

3.3. *Temperature-dependent luminescence properties*

Fig. 10 shows the thermal stability of $Ba_3MSi_8O_{18.5}N:Ce^{3+}$ (1 mol%, M=Mg, Ca, $Sr_{0.6}Mg_{0.4}$, $Sr_{0.6}Ca_{0.4,}$) at excitation wavelength of 330 nm. The relative emission intensity of $Ba_{2.94}MCe_{0.04}Si_8O_{18.5}N$ (M=Mg, Ca, $Sr_{0.6}Mg_{0.4}$,$Sr_{0.6}Ca_{0.4}$) is markedly

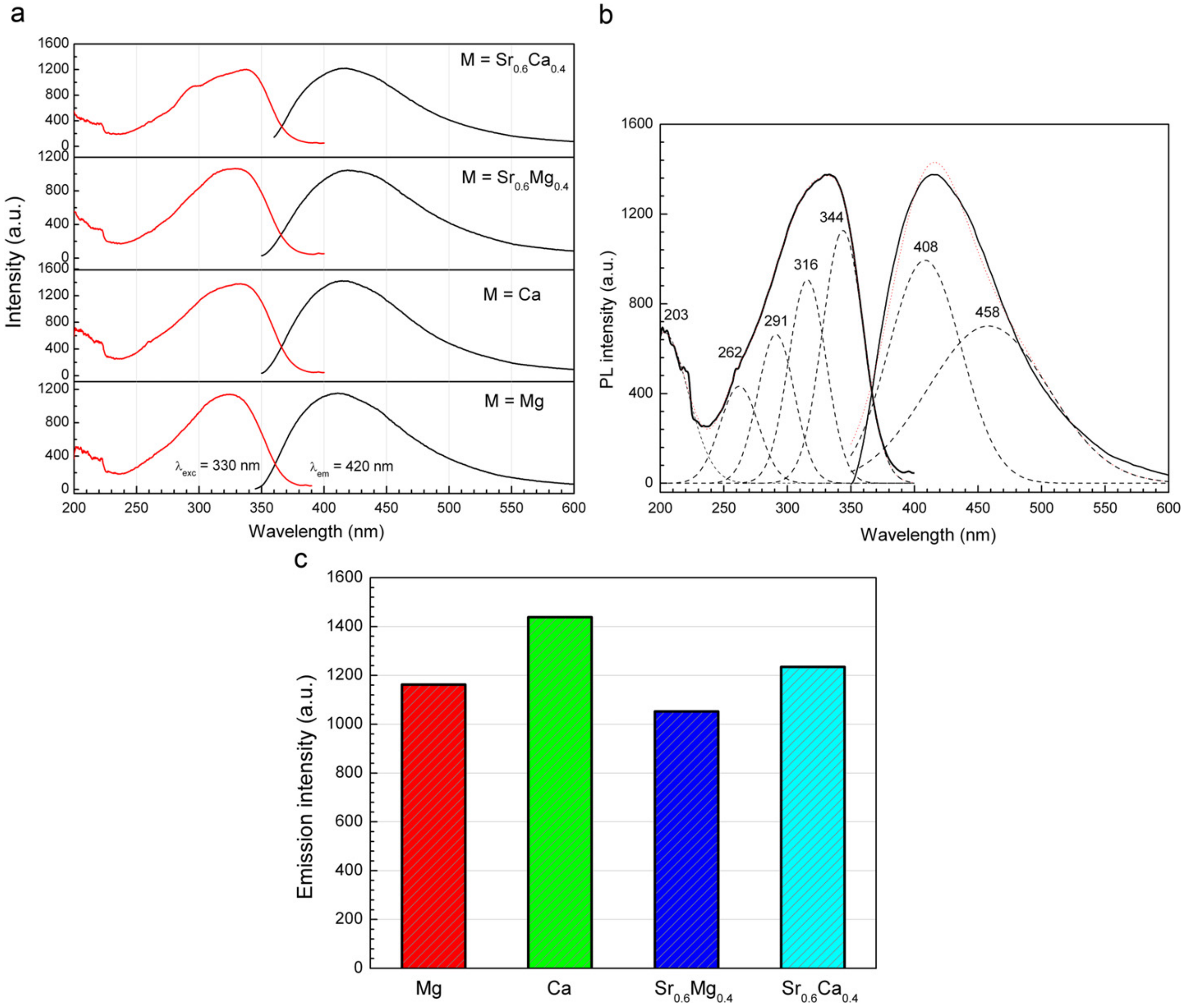

Fig. 8. (a) Excitation and emission spectra of $Ba_{2.94}MCe_{0.04}Si_8O_{18.5}N$ (M=Mg, Ca, $Sr_{0.6}Mg_{0.4}$, $Sr_{0.6}Ca_{0.4}$). (b) Excitation and emission spectra with the deconvolve Gaussians of $Ba_{2.94}CaCe_{0.04}Si_8O_{18.5}N$. (c) Relative emission intensity varying with the type of M.

decreased following an exponential decay model. At 150 °C, the residual emission intensity of $Ba_3MSi_8O_{18.5}N$:Ce^{3+} (1 mol%) is about 50% of its initial intensity at room temperature. Moreover, the thermal quenching rate decreases with varying M in the sequence of $Sr_{0.6}Mg_{0.4} > Ca > Mg > Sr_{0.6}Ca_{0.4}$, corresponding to a decrease of the thermal quenching temperature ($T_{1/2}$: the temperature with half initial emission intensity at room temperatures) (see Table 5). In a way of dual-substitution, M=$Sr_{0.6}Ca_{0.4}$ has the best thermal stability. The thermal quenching rate of $Ba_3MSi_8O_{18.5}N$:Ce^{3+} may be associated with the onset of the absorption edge of the phosphor, as indicated in Fig. 6 and Table 5, which suggests that the higher the absorption edge in energy, the better the thermal stability of $Ba_3MSi_8O_{18.5}N$:Ce^{3+}. This may be explained by the fact that the activation energy of ionization of Ce^{3+} is relatively small due to the virtual conduction bands, i.e., the topmost 5d bands of Ce^{3+} plus the bottom of the conduction band of the host, at the lower energy levels.

4. Conclusions

Ce^{3+}-doped $Ba_{4-z}M_zSi_8O_{20-3x}N_{2x}$ (M=Mg, Ca, $Sr_{0.6}Mg_{0.4}$, $Sr_{0.6}Ca_{0.4}$) phosphors were synthesized by a solid-state reaction at the temperature of 1050–1300 °C in a N_2/H_2 atmosphere. Through partial replacement of O with N in the host lattice of $Ba_2Si_4O_{10}$ with a combination of M substitutions, novel silicon oxynitride of $Ba_{4-z}M_zSi_8O_{20-3x}N_{2x}$ (M=Mg, Ca, $Sr_{0.6}Mg_{0.4}$, $Sr_{0.6}Ca_{0.4}$) can be obtained in a limited solid solution form with an orthorhombic structure. Ce^{3+}-doped $Ba_{4-z}M_zSi_8O_{20-3x}N_{2x}$ (M=Mg, Ca, $Sr_{0.6}Mg_{0.4}$, $Sr_{0.6}Ca_{0.4}$) phosphors can be efficiently excited in the spectral range of 300–360 nm and emit blue light with a broad emission band peaking at about 400–445 nm, depending on the type of M and the concentration of Ce^{3+}. With an increase in the concentration of Ce^{3+}, both excitation and emission bands show the red shift because of the Ce^{3+}–Ce^{3+} energy transfer and/or reabsorption of Ce^{3+}, as well as the Stokes shift. The best thermal stability was found to be M=$Sr_{0.6}Ca_{0.4}$ in $Ba_{2.94}MCe_{0.04}Si_8O_{18.5}N$.

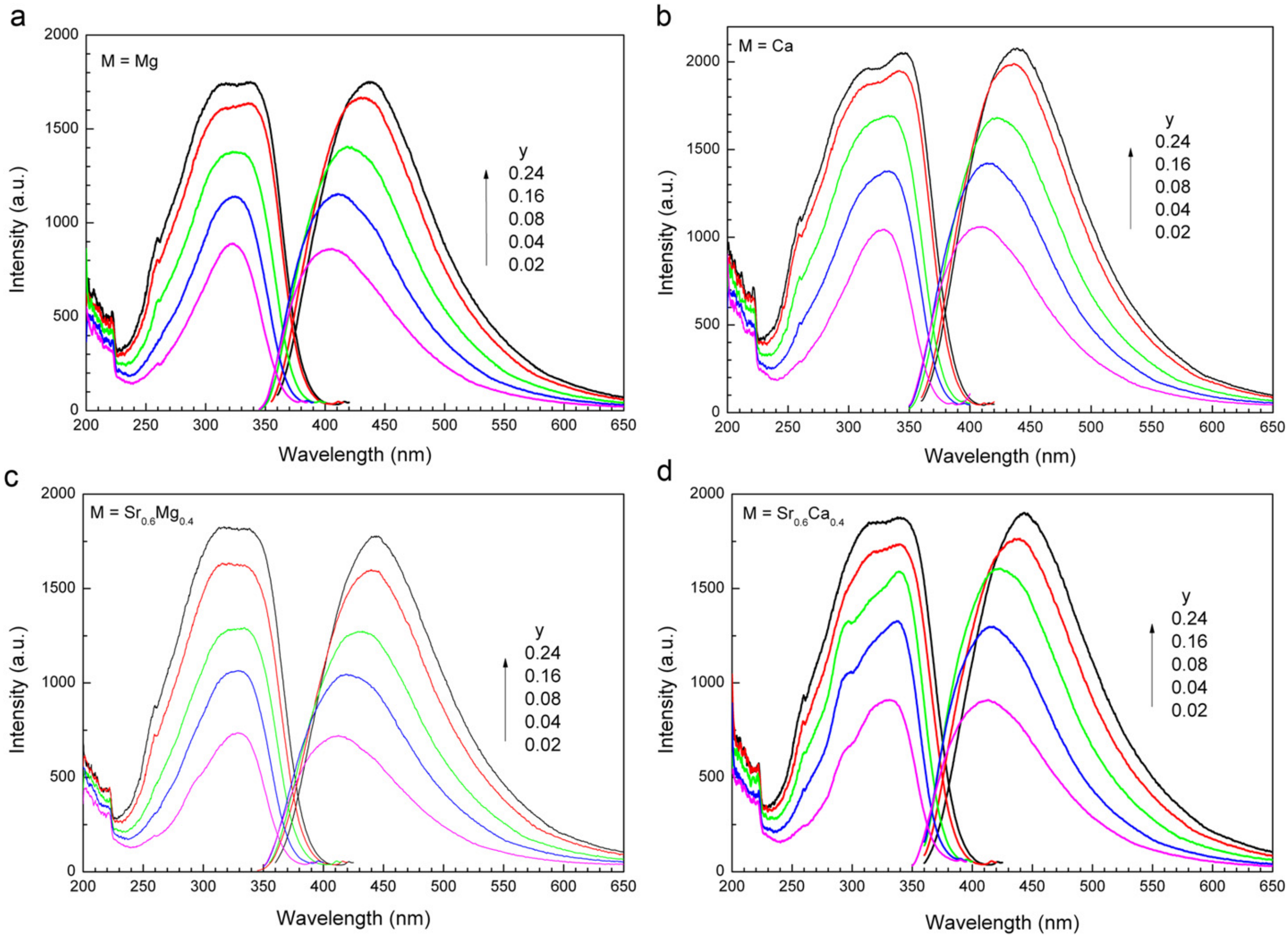

Fig. 9. Photoluminescence spectra with the variation of the Ce^{3+} concentration of $Ba_{3-1.5y}MCe_ySi_8O_{18.5}N$ (M=Mg, Ca, $Sr_{0.6}Ca_{0.4}$, $Sr_{0.6}Mg_{0.4}$).

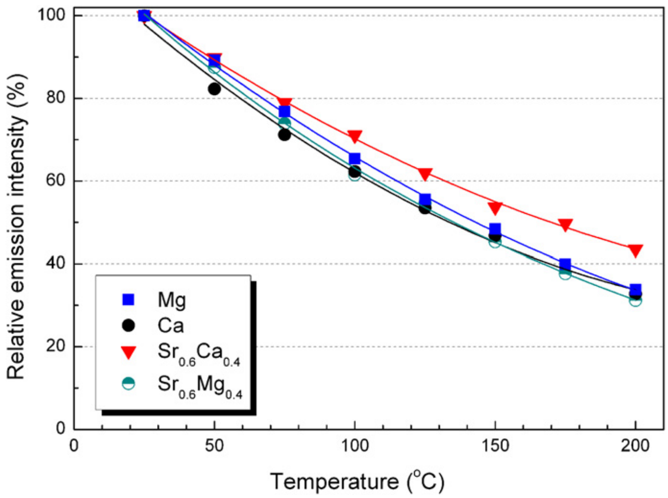

Fig.10. Relative emission intensity of $Ba_{2.94}MCe_{0.04}Si_8O_{18.5}N$ (M=Mg, Ca, $Sr_{0.6}Ca_{0.4}$, $Sr_{0.6}Mg_{0.4}$) as a function of temperature with the excitation wavelength at 330 nm.

Acknowledgment

This work was finically supported by the Natural Science Foundation of Jiangsu Province, China (Project no. BK2008378).

References

[1] J.W.H. van Krevel, H.T. Hintzen, R. Metselaar, A. Meijerink, J. Alloys Compd. 268 (1998) 272.
[2] J.W.H. van Krevel, H.T. Hintzen, R. Metselaar, Mater. Res. Bull. 35 (2000) 747.
[3] R.J. Xie, M. Mitomo, K. Uheda, F.F. Xu, Y. Akimune, J. Am. Ceram. Soc. 85 (2002) 1229.
[4] J.W.H. van krevel, J.W.T. van Rutten, H. Mandal, H.T. Hintzen, R. Metselaar, J. Solid State Chem. 165 (2002) 19.
[5] H.T. Hintzen, Y.Q. Li, Encyclopedia of Materials Science and Technology, Elsevier Science Ltd., 2004, pp. 1–3.
[6] Y.Q. Li, A.C.A. Delsing, G. de With, H.T. Hintzen, Chem. Mater. 17 (2005) 3242.
[7] R. Mueller-Mach, G. Mueller, M.R. Krames, H.A. Hoppe, F. Stadler, W. Schnick, T. Juestel, P. Schmidt, Phys. Status Solidi (A) 202 (2005) 1727.
[8] C. Feldmann, T. Justel, C.R. Ronda, P.J. Schmidt, Adv. Funct. Mater. 13 (2003) 511.
[9] a K. Uheda, S. Shimooka, M. Mikami, H. Imura, N. Kijima, 214th ECS Meeting, Hawaii, 2008.;
b M. Mikami, S. Shimooka, K. Uheda, H. Imura, N. Kijima, Key Eng. Mater. 403 (2009) 11;
c C. Braun, M. Seibald, S.L. Börger, O. Oeckler, T.D. Boyko, A. Moewes, G. Miehe, A. Tuckes, W. Schnick, Chem. Euro. J. 16 (2010) 9646.
[10] R.J. Xie, N. Hirosaki, Y.Q. Li, T. Takeda, J. Lumin. 130 (2010) 266.
[11] Y.Q. Li, G. de With, H.T. Hintzen, J. Mater. Chem. 15 (2005) 4492.
[12] Y.Q. Li, G. de With, H.T. Hintzen, J. Electrochem. Soc. 153 (2006) G278.
[13] Y.Q. Li, N. Hirosaki, R.J. Xie, M. Mitomo, Sci. Technol. Adv. Mater. 8 (2007) 607.
[14] M. Mikami, H. Imura, K. Uheda, N. Jijima, H. Matsuo, Y. Miyamoto, H. Yamamoto, 56th Japan Society of Applied Physics, Spring Meeting, Tsukuba, Japan, March 30– April 2, 2009, p. 1486.
[15] Y.Q. Li, Y. Fang, N. Hirosaki, R.J. Xie, L.H. Liu, T. Takeda, X.Y. Li, Materials 3 (2010) 1692.
[16] K.F. Hesse, F. Liebau, Z. Kristallogr. 153 (1980) 33.
[17] R.M. Douglas, Am. Miner. 43 (1958) 517.

[18] a S.H.M. Poort, H.M. Reijnhoudt, H.O.T. van der Kuip, G. Blasse, J. Alloys Compd. 241 (1996) 75;
  b S.H.M. Poort, A. Meyerink, G. Blasse, J. Phys Chem. Solids 58 (1997) 1451;
  c T. Nakanishi, S. Tanabe, J. Light Vis. Environ. 32 (2008) 93.
[19] A.C. Larson, R.B. Von Dreele, Report LAUR 86-748, Los Alamos National Laboratory, Los Alamos, NM, 2000.
[20] B.H. Toby, J. Appl. Cryst. 34 (2001) 210.
[21] G. Blasse, B.C. Grabmaier, Luminescent Materials, Springer-Verlag, Berlin, 1994.
[22] W.M. Yen, S. Shionoya, H. Yamamoto, Phosphor Handbook, 2nd ed., CRC Press, Boca Raton, 2006.
[23] R.D. Shannon, Acta Cryst. A32 (1976) 751.